13.56 MHz Triple Mode Rectifier Circuit With Extended Coupling Range for Wirelessly Powered Implantable Medical Devices

Yasemin Engür, *Student Member, IEEE*, H. Andaç Yiğit, and Haluk Külah, *Member, IEEE*

***Abstract*—In this work, a wide input/output range triple mode rectifier circuit operating at 13.56 MHz is implemented to power up medical implants. The proposed novel multi-mode rectifier circuit charges the load for an extended coupling range and eliminates the requirement of alignment magnets. The charging process is achieved in three different modes based on the voltage level of the received signal affected by the distance and the alignment of the inductively coupled coils. Current mode (CM) circuit is activated for loosely coupled coils whereas voltage mode (VM) rectification is proposed for high coupling ratios. Extended coupling range is covered with the activation of half wave rectification mode (HWM) in between CM and VM. The rectifier circuit utilizes these three modes in a single circuit operating at 13.56 MHz according to the receiver signal voltage. The circuit is implemented in TSMC 180 nm BCD technology with 0.9 mm^2 active area and tested with printed coils. According to the measurements, the circuit operates in the received power range of 4 to 57.7 mW, which corresponds to 0.10–0.42 coupling range. The maximum power conversion efficiency (PCE) of each operation mode is 51.78%, 82.49%, and 89.34% for CM, HWM, and VM, respectively, while charging a 3.3 V load.**

***Index Terms*—Current mode, extended coupling range, half wave rectification, implantable medical devices, magnet-free operation, triple mode rectification, voltage mode, wireless power transfer.**

I. Introduction

WIRELESS power transmission (WPT) is commonly used in biomedical applications such as cochlear implants [1], [2], retinal prosthesis [3], [4], and neural recordings [5]. These implants require high power for neuron stimulation within a limited volume. This power requirement is satisfied by implantable rechargeable batteries. However, the limited energy of batteries restricts their lifetime and they need to be recharged periodically for long lasting operation [6].

Among WPT systems, capacitive coupling is one of the commonly used method in moderate and high power applications ($\sim$ tens of mWs) [7]–[9]. Power and data transmission are achieved by means of the electrical field between the parallel plates. For low and middle power applications, a more suitable method can be preferred for power transfer such as inductive coupling, which offers high speed charging process within a limited space. Fig. 1 shows the general two-coil inductive RF link system. In this system, transmitter coil (T_X) in the transmitter (primary) side transfers the amplified source voltage to the receiver coil (R_X) in the receiver (secondary) side so that the received signal can be rectified and regulated for use in the implanted device underneath the skin. In power transmission, coupling (k) (transmission rate of the power) is affected by T_X-R_X coil sizes, distance between the link, misalignment, and rotations at the center of the coils. Hence, performance of the WPT system is directly affected from coupling coefficient. To maximize the performance, magnets are used for alignment in conventional devices. Unfortunately, these magnets [10] make implants magnetic resonance imaging (MRI) incompatible so patients with implants need a medical operation before and after the MRI scan to remove and replace the magnets. On the other hand, elimination of magnets makes the coupling coefficient vulnerable to changes in distance between coils and misalignment. Besides, common rectifier circuits cannot operate under variable coupling coefficients. For a magnet free WPT system, multi-mode rectifier circuit is needed. This multi-mode rectifier circuit should rectify the AC signal adaptively for different input levels to compensate coupling change. In addition to coupling

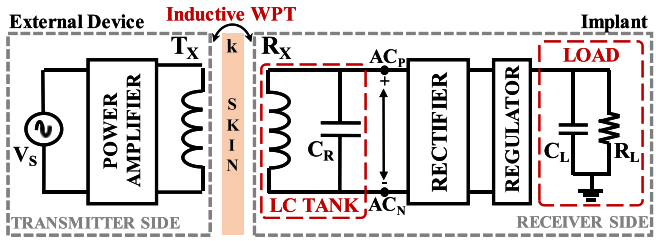

Fig. 1. Schematic of a general WPT system with two-coil RF link structure followed by an AC-DC rectifier and a voltage regulator.

Manuscript received September 28, 2020; revised November 8, 2020 and December 17, 2020; accepted December 18, 2020. Date of publication December 25, 2020; date of current version March 30, 2021. This work was supported by the European Research Council (ERC) through the European Union's Horizon 2020 Research and Innovation Programme under Grant 682756. *(Corresponding author: Yasemin Engür.)*

Yasemin Engür and H. Andaç Yiğit are with the Department of Electrical and Electronics Engineering, Middle East Technical University, Ankara 06800, Turkey (e-mail: yengur@metu.edu.tr; ayigit@metu.edu.tr).

Haluk Külah is with the Department of Electrical and Electronics Engineering, Middle East Technical University, Ankara 06800, Turkey, and also with the METU- MEMS Research and Application Center, Ankara 06800, Turkey (e-mail: kulah@metu.edu.tr).

Color versions of one or more figures in this article are available at https://doi.org/10.1109/TBCAS.2020.3047551.

Digital Object Identifier 10.1109/TBCAS.2020.3047551

limitations, the rectifier circuit should operate either at 6.78 MHz or 13.56 MHz, according to Industrial Scientific and Medical (ISM) band regulations for medical applications [11]. At these frequencies, delay of the circuits become comparable with the switching time and complicate the rectifier design.

In the literature, different rectification approaches for various applications were proposed. These studies differ according to rectification methods, operation voltage, and frequency. The rectification methods are called voltage mode (VM) rectifiers [12], voltage doublers [13], passive rectification, half wave rectifiers and current mode (CM) rectifiers [14]. In VM operation, R_X coil and the resonance capacitance C_R construct an LC tank in the receiver. In [15]–[17], AC-DC conversion is achieved through cross-coupled PMOS switches and an active diode connected NMOS pair. Similarly, [18] and [19] use the same PMOS and NMOS couple with active feedback structure. The feedback circuit compensates the propagation delay coming from the comparators and adaptively changes the drivers of the NMOS switches. Instead of cross-coupled PMOS pair, latched NMOS pair is used in [20] for rectification. Together with the active rectification methods, passive rectifiers and voltage doubler circuits are used in [21] and [22]. These methods can be used for high coupling ratios. Although large amount of power can be transferred using this technique, misalignment effects distort the operation due to decrease in the coupling between the coils, which decreases input power. Also, the power rating (0.5 W- 6 W) and coil sizes make this design unsuitable for use in medical applications [22]. For misaligned and rotated coils with low coupling ratios, CM operation is utilized to rectify AC signal. In this mode, a series LC tank is used in the receiver side to charge the battery/load. CM is reported in different designs [23]–[25]. While [23] aims to improve voltage conversion ratio, [24] offers a very low output power design which cannot be used for high power applications. Furthermore, operation frequencies of 1 MHz [23] and 50 kHz [24] are not suitable for medical applications according to ISM band. In addition to these designs, [25] proposes a voltage-boosted CM operation to charge a 1.1 V battery at 6.78 MHz. However, the single mode studies above, be it VM or CM, cover only a small coupling range resulting from the elimination of alignment magnets. To cover an extended coupling range, a mixed mode rectifier circuit is needed. The mixed mode idea is presented in [26] by switching the operation between VM and CM according to the receiver voltage on R_X. Power range of 0.1–20 mW can be covered with this design, but the operation frequency of 1 MHz does not satisfy the frequency requirement determined by ISM band regulations. The dead zone between the VM-CM is eliminated in another design [27]. Yet, these circuits cannot be used in medical applications due to coil sizes and operation frequency limitations.

In this paper, a magnet free extended range triple mode rectifier circuit operating at 13.56 MHz is proposed and implemented to power up implantable medical devices. The main challenges of this design are the operation frequency, and variable input power level. The proposed rectifier circuit includes multi operation modes which are voltage mode (VM), half wave mode (HWM) and current mode (CM) operations and high-speed comparators to overcome these challenges. According to the best of our knowledge, extended coupling range triple mode circuit is the first mixed mode rectification method at 13.56 MHz operation frequency which makes it suitable for medical applications.

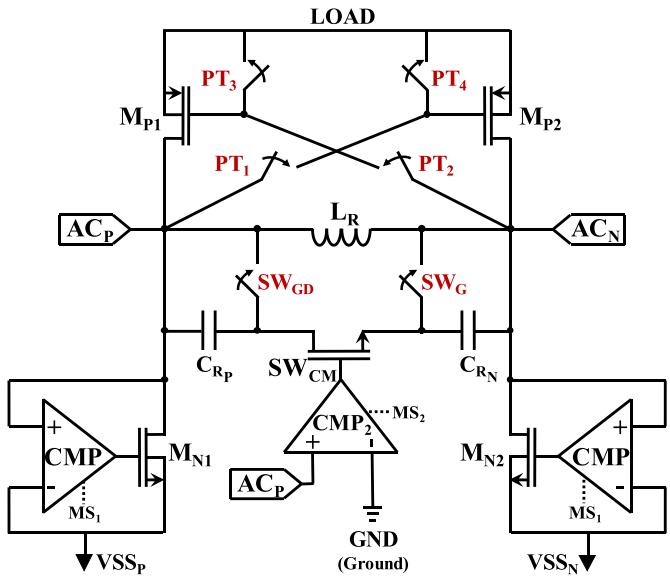

Fig. 2. Schematic of the proposed triple mode rectifier circuit.

The organization of this paper is as follows: The operation principle of each mode and the circuit implementation is discussed in Section II. The measurement results of the triple mode circuit including the in vitro tests and the comparison with the state of the art are presented in Section III. Finally, Section IV concludes the work with discussions.

II. Triple Mode Rectifier Design And Circuit Implementation

The triple mode rectifier schematic for biomedical implants is illustrated in Fig. 2. In the design, cross-coupled PMOS switches, active diode connected NMOS pair and current mode control switch form the main schematic. To get the maximum power conversion efficiency, different modes are activated for different couplings. While CM and HWM use a single ended AC signal, VM rectifies floating AC signal as a full wave rectifier. Therefore, the layout of the overall circuit is drawn symmetrically with respect to the axis of symmetry passing through the switch SW_{CM}. This allows each half of the circuit to match with the other half, improving VM efficiency. For that purpose, resonance capacitor is divided into two equal capacitances, C_{RP} and C_{RN}. Similarly, the dummy grounding switch (SW_{GD}) is used to preserve symmetry with the grounding switch (SW_G) utilized in CM.

Charging process starts with the generation of *MODE SELECT 1 (MS_1)* and *MODE SELECT 2 (MS_2)* signals in the control block (Fig. 3(a)). These signals, which are determined by the input voltage level, control the operation mode of the circuit. For high voltages (coupling ratios) MS_1 signal become low and the circuit is in VM mode. When the control block sets MS_1 to high, the circuit operates either in CM or HWM. For

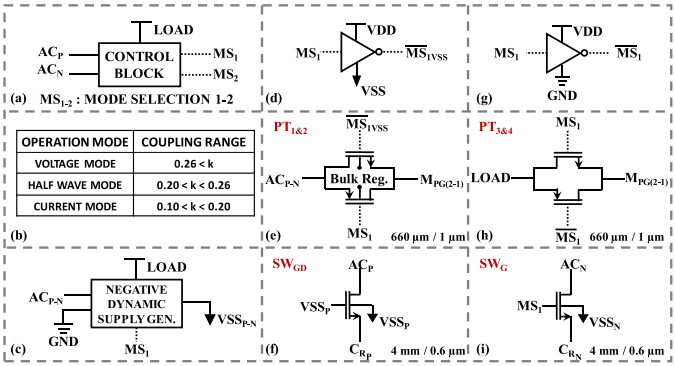

Fig. 3. (a) Mode signal generation from the decision unit, (b) operation modes and coupling coefficient relation, (c) *VSS* generator block diagram, (d) $\overline{MS_{1VSS}}$ signal generator, (e) schematic of $PT_{1\&2}$, (f) VSS_P controlled dummy grounding switch *(*SW_{GD}*)* between AC_P and C_{RP} nodes, (g) $\overline{MS_1}$ signal generator, (h) schematic of $PT_{3\&4}$, (i) grounding switch *(*SW_G*)* between AC_N and C_{RN} nodes.

low voltage levels (coupling ratios), CM is activated. In CM the coils are loosely coupled, and oscillation is required for charging. HWM is used for mid coupling ratios to rectify AC signal with better efficiencies between VM and CM. Utilization of these three modes enables operation for an extended range coupling ratio (Fig. 3(b)).

In this WPT circuit, there is only one power supply, called *LOAD*, and it is charged by the rectifier. However, when CM or HWM operation is activated, AC signal takes negative values, and this creates a leakage problem to the substrate. To prevent the leakage, negative dynamic supply generator (*NDSG*) is implemented to the system. There are two *NDSG* subblocks in the circuit to maintain the symmetry. One of them takes AC_P and ground (*GND*), while the other one has AC_N and *GND* as inputs. Then, the generated VSS_P and VSS_N voltages are connected to the body terminals of the main NMOS switches M_{N1}, M_{N2}, SW_{GD} (Fig. 3(f)) and SW_G (Fig. 3(i)). In addition to these switches, pass transistor pairs $PT_{1\&2}$ (Fig. 3(e)) and $PT_{3\&4}$ (Fig. 3(h)) are used to switch the configuration of the entire system when the operation mode is decided. Optimization of each switch size is performed to maximize the efficiency of the rectifier and minimize switching losses. Moreover, bulk regulation is added to $PT_{1\&2}$ pass transistors to prevent leakage due to the AC voltage variation. Simulated waveforms of voltage mode, half wave mode and current mode operations are given in Fig. 4(a), (b), and (c), respectively. In each mode, AC signal is rectified to transfer the input power to the *LOAD,* whose voltage is increased in each charging cycles. Control signals of the $M_{N1\text{-}2}$ and SW_{CM} switches indicate the switching times of the charge conduction to the *LOAD*. In addition to the simulation results, measurement results of each mode are provided with the detailed circuit description in the following sections.

A. Voltage Mode Rectifier

Fig. 5 shows the simplified version of the triple mode rectifier circuit for voltage mode operation. When the coils are highly coupled *(*$k > 0.26$*)*, MS_1 signal becomes zero, and receiver power becomes high enough to charge the load. When VM is activated, $PT_{1\&2}$ connect AC signals to PMOS gates and form the cross-coupled structure. At the same time, $PT_{3\&4}$ disconnect the link between *LOAD* and $MP_{1\&2}$ transistors' gates. Besides, CM switch turns on and grounding switches *(*SW_G*&*SW_{GD}*)* are deactivated.

In VM operation, M_{N1}*&*M_{P2} and M_{N2}*&*M_{P1} pairs work synchronously in crosslinked states. When AC_P is in ground level, AC_N is high and M_{P1} turns off. VM control unit forces AC_P to ground during this half period of the oscillation. Hence, M_{P2} turns on, and power is transferred from AC_N to *LOAD*. In the other half, M_{N2} and M_{P1} pair charges the load. During this charging process, NMOS switches are turned on and off by the VM control circuit shown in Fig. 6(a).

The VM subblock is comprised of a common gate comparator *(CG CMP)*, a pulse duration adjustment block, digital control block, and driver circuit. *CG CMP*, preferred for its high-speed operation property, takes AC signal and ground as inputs and finds the zero crossing points by comparing these signals. While designing the comparator, it was observed that there exists a delay between the switching response and the output of *CMP* at the operation frequency of 13.56 MHz. Consequently, like [21] an intentional mismatch is inserted to the differential pair transistors $M_{12\&16}$ and $M_{18\&21}$ as shown in Fig. 6(b). This mismatch at the input pair corresponds to an offset voltage in the comparison. In other words, AC_P is compared with the offset voltage and output is sensed. Switching speed performance of VM comparator in simulations shows that gate control voltage of M_N switches has $\sim$1 ns rising time and $\sim$0.3 ns falling time. In addition, the gate control signal responds to voltage change in AC signal within 4 ns. When the output of the *CMP* becomes high, NMOS switch turns on. To complete the switching, an off path should be introduced to the system. For that purpose, an analog pulse width duration adjustment block (Fig. 6(c)) and SR latch is added. When the output of the *CG CMP* becomes high, the delayed version of the *CG CMP* signal is generated by the delay cell and fed into the latch structure through a digital control unit, which is utilized to reset the circuit as may be required (Fig. 6(d)). When pulse duration adjustment signal *(*T_P*)* becomes low, M_{23} turns on and shorts the *CMP* output to the ground instantly. Meanwhile, T_P cuts off the differential pair current to increase the power efficiency of VM by preventing unnecessary loss of power. As a result, the switching pulse is generated to control the gate voltage of the NMOS switches M_{N1} and M_{N2} at the frequency of 13.56 MHz. In the driver circuit (Fig. 6(e)), three end-to-end connected inverters are utilized, and the size of the transistors are optimized to minimize power loss. Since the coupling ratio determining AC input and *LOAD* voltage change, charging duration is readjusted by the analog current starved delay block. With this block, conduction time can be adjusted externally to maximize the transferred power to obtain maximum power conversion efficiency (PCE) in the rectification.

As the triple mode circuit includes three different rectification modes, enable signals are added to each subblock to improve efficiency and prevent power loss. MS_1 signal either lets the *CG CMP* output to go to the driver or enables an external voltage

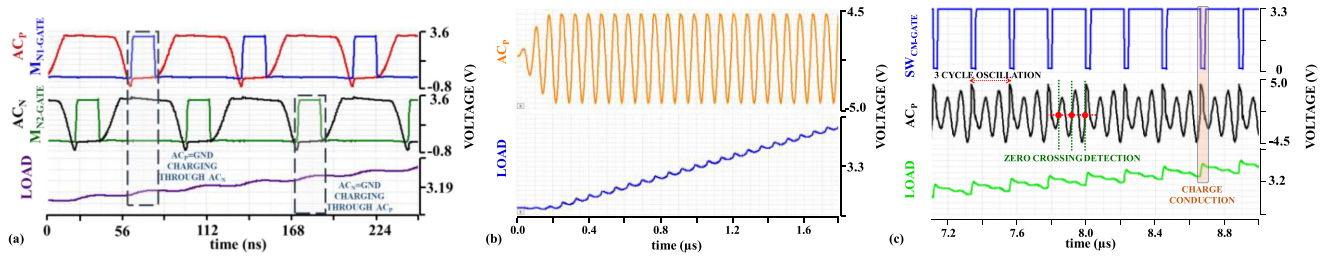

Fig. 4. Simulated control signals and charging waveforms of (a) voltage mode, (b) half wave mode and (c) current mode operations.

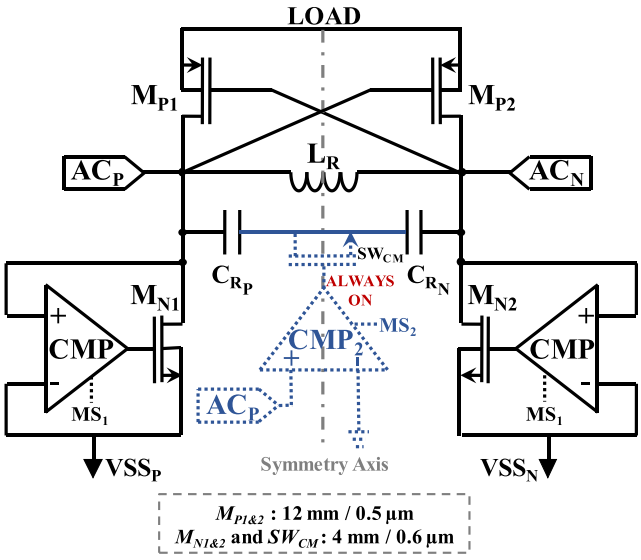

Fig. 5. Schematic of voltage mode operation for high coupling ratios.

to control the gates of the NMOS pairs. Also, MS_1 enables and disables the *CMP* operation, like T_P signal. Fig. 7 illustrates the measured waveforms of differential AC signal $(AC_P - AC_N)$ and one of the NMOS gate control signal $(M_{N\text{-}GATE})$ in VM operation. The peaks of the AC signal are clipped due to charge conduction and each NMOS switch turns on and off each cycle accordingly.

B. Current Mode Rectifier

Inductive link may not result in high coupling ratios all the time, due to the misalignment and angle change between the coils. As the coupling decreases, transmitted power to the receiver side becomes low. When the received signal becomes lower than the *LOAD* voltage, voltage rectification cannot be performed as in VM. Nevertheless, low couplings should be considered for a wide range functional system. Hence, for loosely coupled coils $(0.10 < k < 0.20)$, CM is activated in the triple mode rectifier as shown in Fig. 8. In CM, the cross coupled connection is broken. M_{N1} and M_{P2} pair is deactivated and PT_3 converts M_{P1} switch to diode connection. On the other hand, M_{N2} switch creates a grounding path for LC resonator. In this way, the resonator oscillates on the ground level. The grounding switch of the mode (SW_G) grounds the right side of the inductor and switch by bypassing the C_{RN} capacitor. In this configuration, the circuit becomes ready to charge the load in CM.

Current mode switch (SW_{CM}) is the main part of the operation and is controlled by the driving and controlling comparator CMP_2. When the CM switch is on, AC signal starts to oscillate across the inductor L_R and the capacitor C_{RP} with an increased amplitude. During the oscillation, AC signal grows, and power is stored on L_R. When the voltage on C_{RP} becomes zero, contact between each side of the control switch (SW_{CM}) is disconnected. Thus, the maximized inductor current is transferred to the *LOAD* during the conduction.

As illustrated in Fig. 9(a), AC signal is compared with the ground in a common source comparator (Fig. 9(b)) and zero crossing points are detected. Zero crossing detection is performed to determine the possible switching times by digitalizing the AC turning points. According to simulation results of CM comparator speed analysis, the gate voltage of SW_{CM} has ∼0.4 ns rising and falling times. Also, AC voltage change can be detected with the output of the comparator in ∼2.5 ns. After the digitalization, the signal is shaped by cycle selection unit to decide the oscillation cycle of the AC signal. Cycle selection unit is controlled externally with 3-bit digital inputs. According to the received voltage level, cycle number can be adjusted from 2 to 7 such that the maximum power transfer can be achieved in different couplings. For the couplings close to 0.20, the signal becomes high enough to charge the load, oscillation cycle can be adjusted as 2-4. However, if the input voltage level is low (∼0.10), more cycles are needed to increase the AC signal level to charge the load. After the predetermined oscillation cycle is reached, SW_{CM} turns off and the connection between the C_{RP} and the virtual ground is broken. The accumulated power on the inductor is transferred to the *LOAD* through the M_{P1} diode. To maximize the efficiency and minimize conduction losses, the pulse width of the conduction is controlled by the same current starved delay buffer used in VM for different power levels. Also, using the CM comparator output at the digital control unit, $SW_{CM\text{-}GATE}$ signal is generated with the minimized circuit delays. When the conduction is finalized, SW_{CM} turns on and the AC signal starts to oscillate until the next conduction happens. Measured waveforms of oscillating AC signal and the gate voltage of current mode switch $(SW_{CM\text{-}GATE})$ for 4 cycle oscillation are given in Fig. 9(c). As explained in the figure, once the AC oscillates for 4 cycle, charge conduction occurs, and process is reset, and the circuit begins the next oscillation and

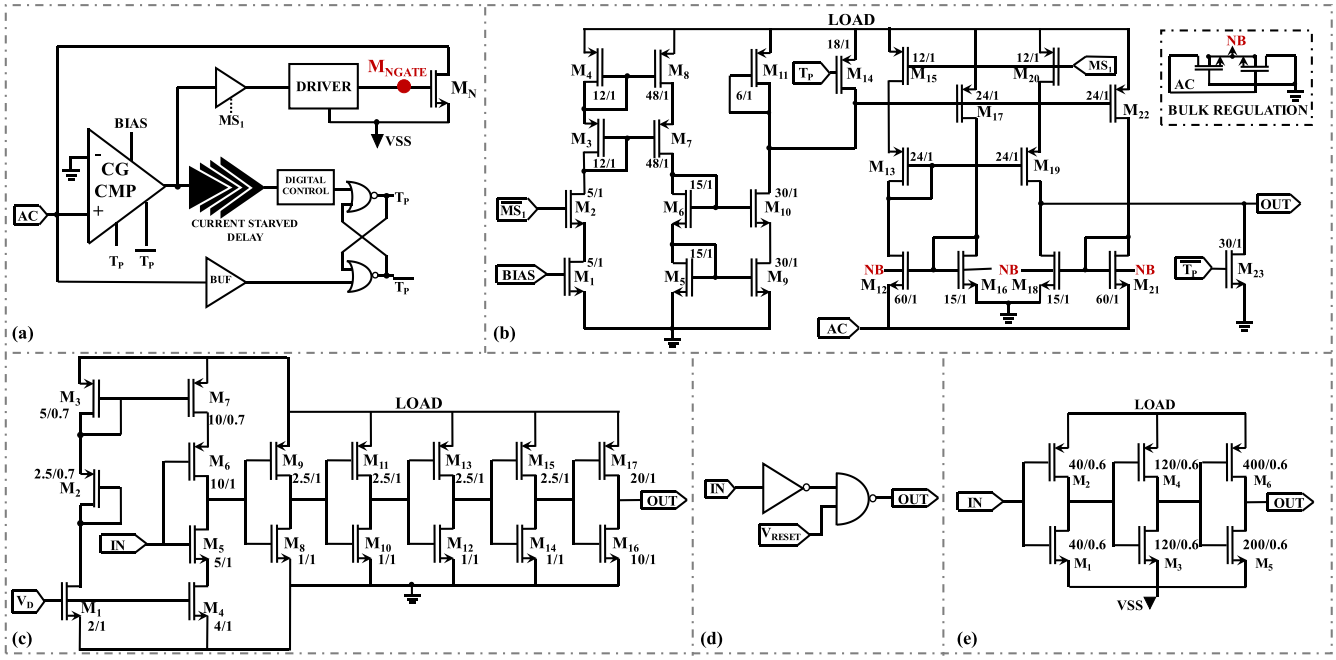

Fig. 6. (a) Voltage mode operation control block including common gate comparator, switching pulse duration adjustment block and the driver, (b) common gate comparator circuit, (c) current starved delay circuit, (d) digital control unit of VM, (e) driver circuit.

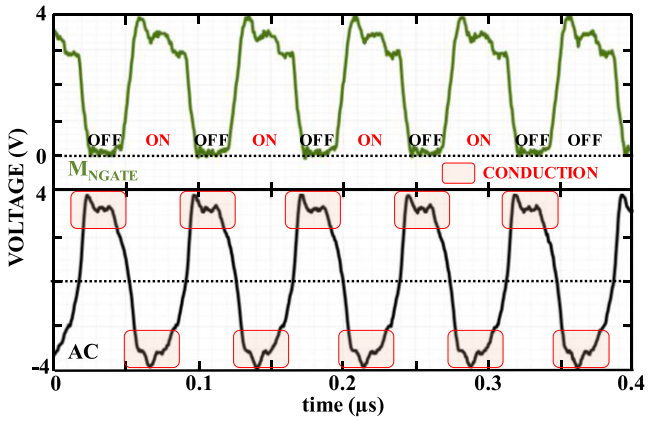

Fig. 7. Experimental results of differential AC $(AC_P\text{-}AC_N)$ signal and gate control voltage of M_N switch (M_{NG}) in VM operation.

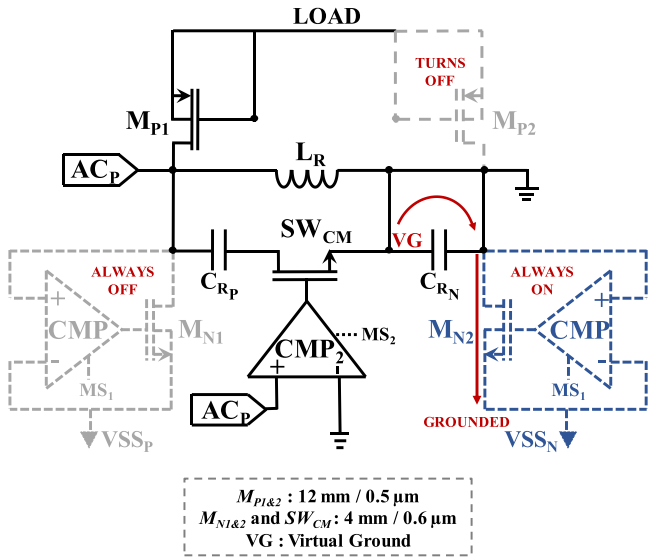

Fig. 8. Schematic of current mode operation for loosely coupled coils in WPT.

charging process. Also, the measured waveform of AC signal for different oscillation cycles is illustrated in Fig. 10.

Compared to the VM operation, CM works under low couplings; hence, low input powers. However, as the coupling increases, received power level increases and multiple cycle oscillation idea loses its meaning. Instead of waiting for oscillations, load can be charged in each cycle. However, the increase in inductor current with coupling causes conduction losses, and single cycle oscillation means the unnecessary power consumption during the activation and deactivation of each subblock and switch in CM. Hence, instead of CM, different rectification method can be preferred to obtain better performance for higher couplings (k $>$ 0.20). At this point, voltage mode should be enabled to increase power conversion efficiency by full wave rectification. Yet, as the increase in coupling is not high enough for the circuit to start operating in VM, a third mode becomes necessary as an intermediate step to increase the efficiency between CM and VM to charge the load.

C. Half Wave Mode Rectifier

Increase in coupling ratio causes a decrease in oscillation cycle. With this reduction, the circuit reaches a point where it will start operating with a single cycle oscillation. Hence, the half wave mode, between the CM and VM, is preferred to charge the *LOAD* as the intermediate step until the VM can start to work.

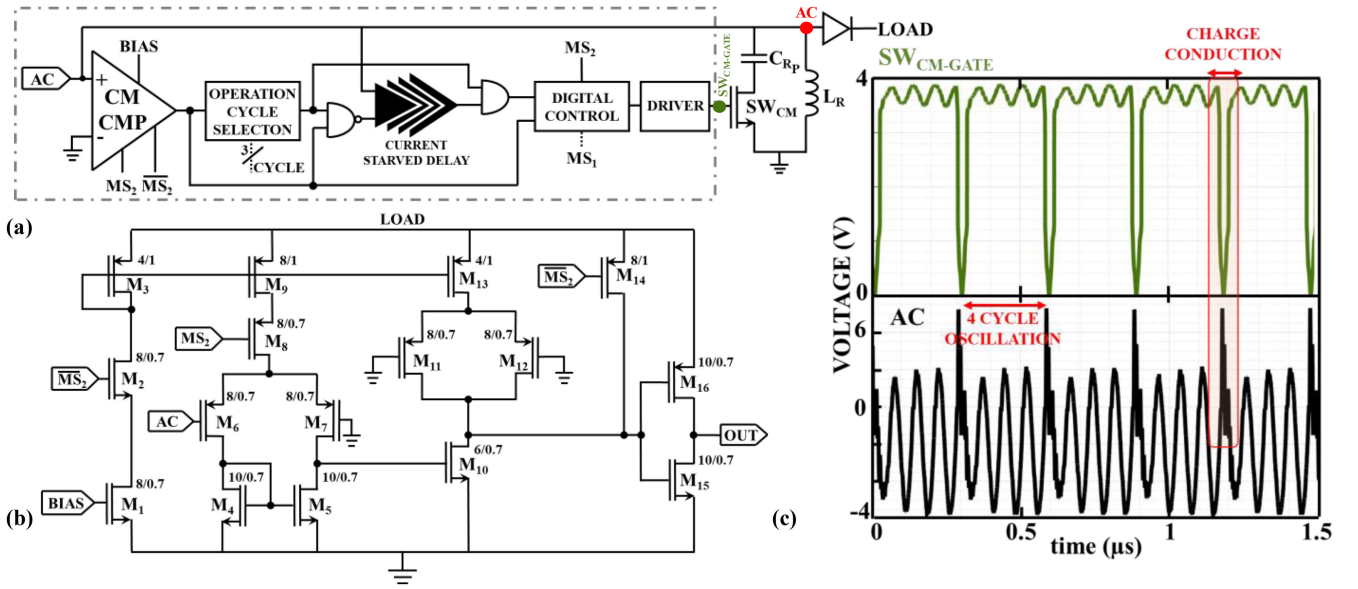

Fig. 9. (a) Current mode control block consisting of CM comparator, cycle selection and bandwidth selection units, digital control blocks and the switch with its driver, (b) internal structure of the current mode comparator *(CM CMP)*, (c) measured waveforms of the gate voltage of the SW_{CM} and AC signal on R_X.

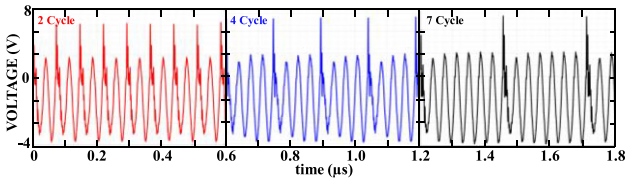

Fig. 10. Measurement results of the oscillating AC signal waveform for 2, 4 and 7 cycle operations in CM.

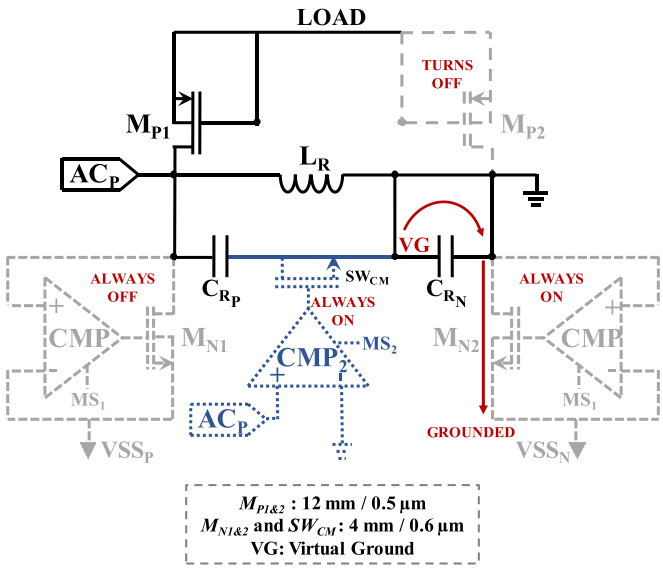

Fig. 11. Schematic of the half wave rectification as an intermediate step in WPT.

HWM rectifier is obtained from CM using the MS_2 signal between the coupling ratios $0.20 < k < 0.26$ as shown in Fig. 9(a). Once the MS_2 becomes one, CM is switched to HWM (Fig. 11). In this mode, SW_{CM} is always on and connects C_{RP} to the virtual ground. Half wave rectification is performed with the LC tank and current flows through the M_{P1} diode to power up the *LOAD*. Compared with CM, complexity of the system is decreased, unnecessary power consumption is eliminated, and HWM gives higher power efficiencies. A drawback of HWM is the diode connected M_{P1} transistor, which causes a voltage drop and limits the power efficiency. In addition, when the peak-to-peak voltage of the received signal increases, the lifetime of the transistors are limited, and an unsafe condition is created. For this reason, the switching from the intermediate step to VM is done for larger coupling ratios.

D. Control Block

Fig. 12(a) shows the block diagram of the control unit. At the beginning of the charging process, rectifiers are not active, and mode selection is performed according to the output of the control block. MS_1 and MS_2 signals are generated using the voltage levels of the *LOAD* and AC signals. The peak detection of the AC is done using the floating AC_P and AC_N signals. A negative voltage converter is used to obtain the DC correspondence of the received AC voltage (Fig. 12(b)). During this voltage conversion, a voltage drop occurs in the peak voltage due to the diode connected transistors. To compensate this drop and have a precise comparison with the *LOAD* voltage, a diode ladder is used (Fig. 12(c)).

Comparison is performed with a hysteresis comparator and the output is connected to logic block. If the *LOAD* becomes larger than AC, CM is activated. Contrarily, if *LOAD* voltage becomes smaller than AC signal, MS_1 and MS_2 signals are adjusted according to the coupling level, i.e., voltage level of the AC signal. The peak detector output is compared with an externally

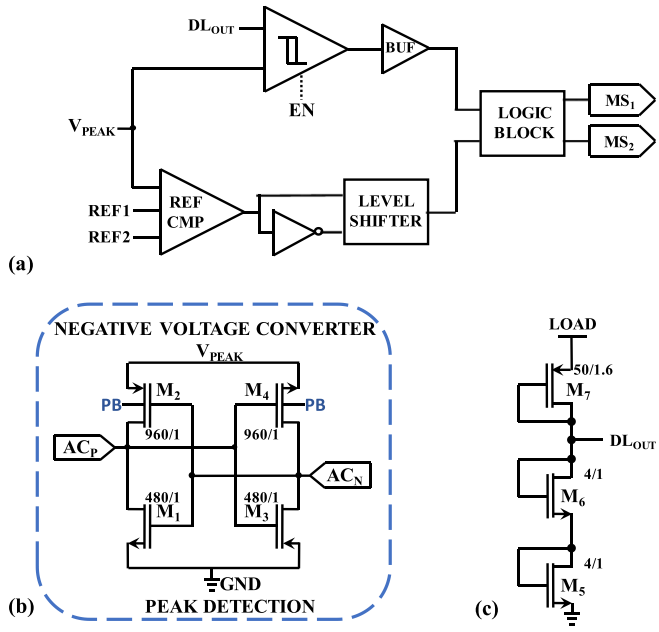

Fig. 12. (a) Block diagram of the control unit, (b) negative voltage converter circuit, (c) diode ladder circuit.

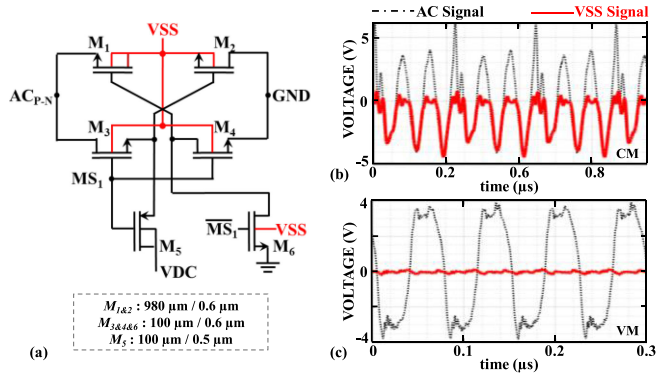

Fig. 13. (a) Circuit schematic of negative dynamic supply generator, experimentally measured *VSS* and AC signal waveforms for (b) CM and (c) VM modes.

adjusted reference voltage, V_{REF}. The output becomes one for the signals smaller than V_{REF} and zero for signals larger than V_{REF}. In other words, if the *LOAD* is smaller than AC signal and $V_{PEAK\text{-}AC}$ is smaller than V_{REF}, MS_1 and MS_2 signals become one, and HWM operates. Otherwise, V_{LOAD} is smaller than $V_{PEAK\text{-}AC}$ and $V_{PEAK\text{-}AC}$ is larger than V_{REF}, MS_1 and MS_2 signals become zero, and VM is activated.

E. Negative Dynamic Supply Generator

In the proposed work, different modes are combined in a single circuitry. Since the AC oscillates and takes negative values in CM and HWM, possible leakage and reverse current to the bulk of the transistors should be prevented. To this end, bulk regulation is required and a negative dynamic supply generator *(NDSG)* is added to the overall system (Fig. 13(a)) based on a standard bulk regulation circuit. The *NDSG* circuit operation is controlled by MS_1 signal. The circuit operates as a standard

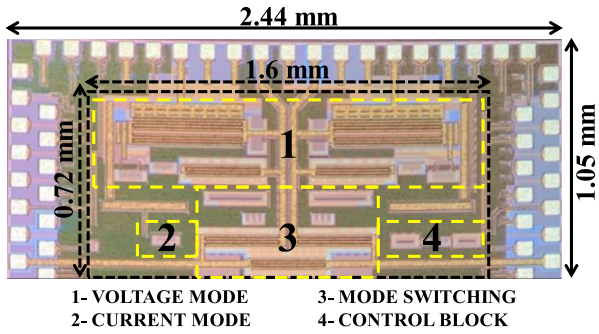

Fig. 14. Fabricated chip micrograph of the proposed triple mode rectifier occupying 0.9 mm^2 active area (1.15 mm^2 with test circuitry and 2.56 mm^2 with pads).

bulk regulator in CM and HWM. However, in VM, transition time of the switches are less than the delay of the standard bulk regulation circuit. Therefore, the power efficiency drops significantly with the standard bulk regulation circuit. Furthermore, the AC voltages are clipped by the circuit operation and do not become negative. To prevent power loss, the *NDSG* circuit shorts the negative supply to ground in VM. By mode dependent dynamic supply, negative supply is generated according to the input voltage level.

In CM and HWM, the *NDSG* circuit compares AC signal with ground level *(GND)* and follows the lowest voltage. $M_{5\&6}$ turn off with MS_1 signal and $M_{3\&4}$ control the gate voltages of $M_{1\&2}$. The measurement result of the *NDSG* circuit in CM can be seen from Fig. 13(b). The generated negative signal *(VSS)* follows the most negative signal and prevents the bulk leakage. In the full wave rectification mode, i.e., VM, $M_{5\&6}$ are activated to turn $M_{3\&4}$ off. M_2 becomes always on, and M_1 turns off. AC changes between the ground level and the positive voltages. As a result, the *NDSG* gives the most negative voltage which is ground *(GND)*. Fig. 13(c) shows the experimental results of AC signal and the generated negative signal for VM. With the *NDSG* circuit, the VM efficiency is not affected from required bulk regulation for the other modes.

III. Experimental Results

The triple mode rectifier circuit is implemented in TSMC 180 nm BCD technology. Fig. 14 shows the chip micrograph of the design with the floor plan. The floor plan consists of voltage mode rectifier, current mode rectifier (including half wave mode), VM-CM switching circuitry and the control block of the system with an active area 0.9 mm^2. During the measurements, the experimental setup shown in Fig. 15(a) is used. In the test setup, a custom designed coil pair is used for power transfer. A signal generator is used to give input to T_X coil. Also, the DC supply is used to bias comparators and delay buffers and to supply voltage to electrostatic discharge (ESD) diodes for the safety of the chip. To avoid grounding problems, AC and DC grounds are isolated from each other. Finally, the oscilloscope monitors the results obtained from the chip test PCB.

The chip is tested with the printed board coil pair in different coupling ratios. The coil pair is designed in ANSYS EM to

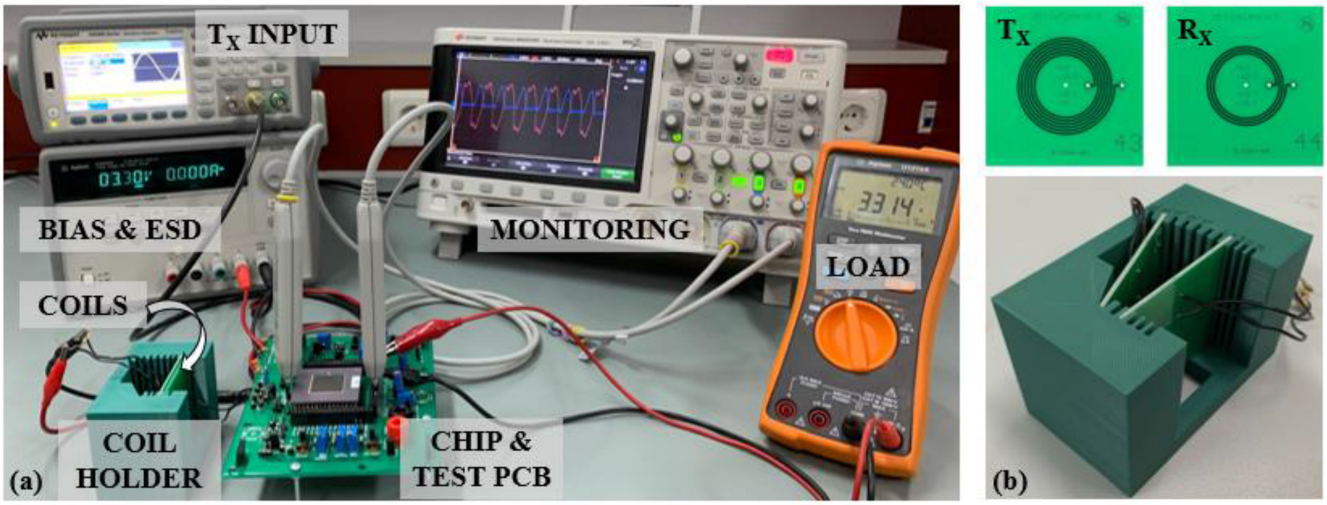

Fig. 15. (a) Experimental setup of the triple mode rectifier operating at 13.56 MHz, (b) T_X and R_X coils with the coil holder.

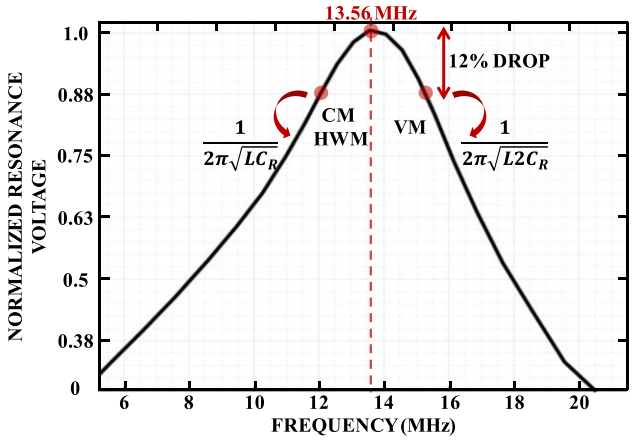

Fig. 16. Resonance capacitance selection through measurements.

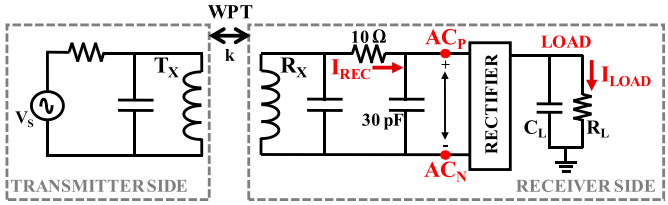

Fig. 17. Input and output power measurement setup.

maximize the coupling ratio between the coils without using an alignment magnet as explained in the previous work [28]. Coil holder helps to change the position of the coils horizontally. Also, an intentional angle can be introduced to the system to observe misalignment effects. Coil and the holder are given in Fig. 15(b). (1) defines the coupling coefficient which is the ratio of R_X and T_X voltages. During the measurements, the single coil pair is used with different coupling ratios provided by the position change.

$$\text{Coupling} \quad (\text{k}) = \frac{\text{Received Voltage on R}_\text{X}}{\text{Transmitted Voltage on T}_\text{X}} \qquad (1)$$

In this design, two C_R capacitors are used to preserve the symmetry of the system. As shown in Fig. 16, the normalized resonance voltage at the receiver side makes a peak at 13.56 MHz for the perfectly matched resonance capacitor (156 pF). However, in the proposed system, single C_R is used for CM and HWM, and two series connected C_R is used for VM operation. Therefore, the resonance capacitor C_R is chosen as 220 pF by considering parasitic capacitances. In this way, the peak resonance capacitance is the geometric mean of the two operation capacitances, which are 220 pF and 110 pF. By considering the 12% total efficiency drop, we have minimized the switching losses while combining the three different modes in a single circuit.

In the measurements, 13.56 MHz sinusoidal constant amplitude signal is given to the transmitter coil and the power is transferred to the receiver side. At the receiver side, resonator structure is captured the transmitted AC signal. According to the received signal level, related operation mode is activated externally by the help of the generated MS_1 and MS_2 signals.

Tests are performed from low to high coupling ratios and AC signals are observed. For each coupling coefficient, *LOAD* voltage is set to 3.3 V by calibrating the load resistance of the system manually, and input and output powers are recorded. While the load resistance is changed, the load capacitance (C_L) is kept constant at 4.7 μF. During the input power measurements, the measurement method proposed in [16] is used (Fig. 17). Two differential probes are used to observe the AC signal and the rectifier current. A 10 Ω sampling resistor and a 30 pF compensation capacitor are used to observe the input current (I_{REC}), and the differential AC (AC_P-AC_N) input voltage. Using the measured current and the voltage values the input power is calculated. In these calculations, rectifier current is taken into consideration instead of the LC current. Hence, using a sampling resistor affects the power on LC tank, but it does not cause change in the rectifier power. As a result, the power conversion efficiency is obtained without measurement setup distortion. Fig. 18 shows the measured output power and power conversion efficiency of

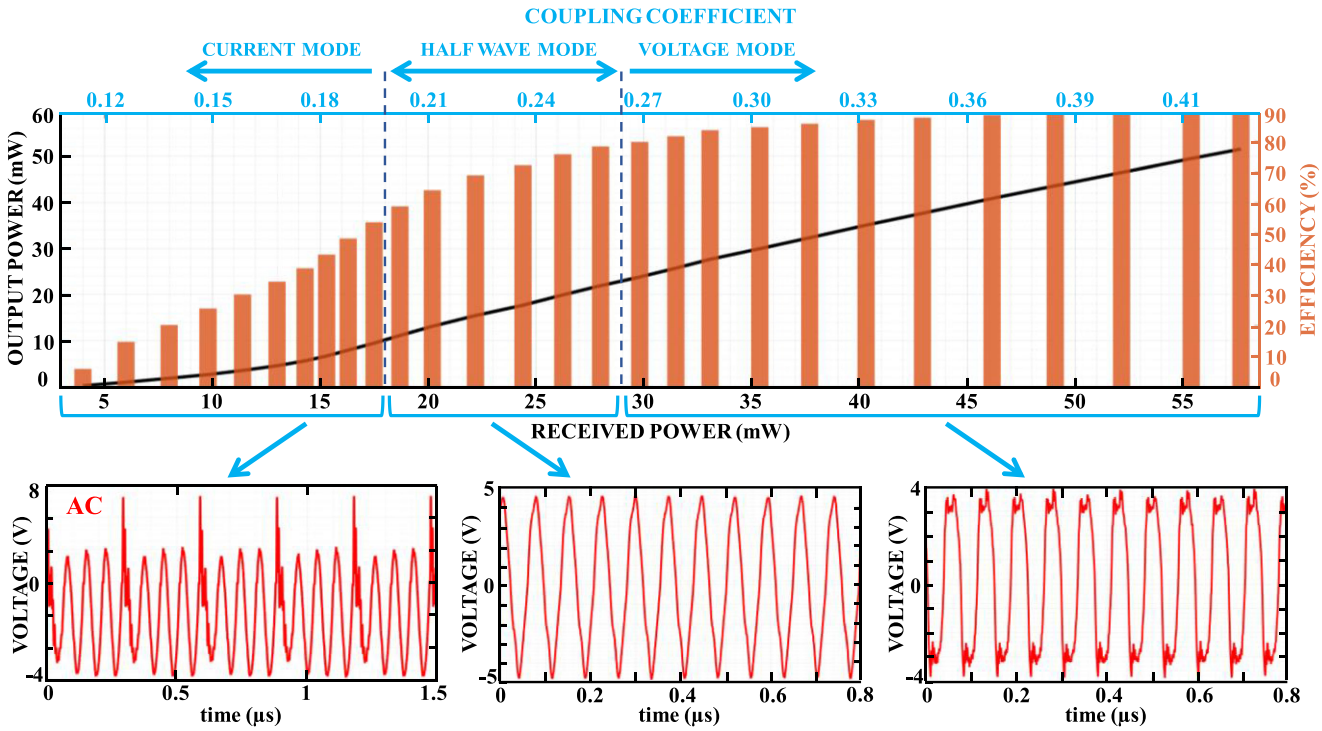

Fig. 18. Measurement results of output power and power conversion efficiency of the triple mode rectifier circuit for different received power values, and the AC voltage waveform examples for each operation.

the triple mode rectifier circuit with respect to different received signal powers. The PCE tests are performed with a constant T_X power by changing the coupling coefficient. The system can operate with different coil distances (2 mm to 10 mm) and misalignments (0° to 20° angle variations).

In CM, rectified input power starts from 4 mW with the corresponding output power of 233 μW and increases up to 17 mW with an output power of 8.8 mW. Maximum power efficiency for CM is 51.78%. Compared with other rectification methods, CM provides lower power efficiencies. This is due to the power consumption of the circuit, which becomes comparable to the output power. Also, in CM, *LOAD* can only be charged in once cycle for each different number of oscillations whereas charge conduction is achieved in each cycle of VM. This causes power efficiency drops. However, medical implants consume low power and 8.8 mW output power with 51.78% efficiency becomes important when there is no other rectification method. When the boundary between the CM–HWM is reached, AC signal grows enough to charge the *LOAD* each oscillation cycle. Accordingly, half wave mode is activated to obtain higher power efficiencies. This mode constructs a bridge between the CM and VM, and HWM enables the overall system to cover the power and the coupling range. For HWM, input power changes from 18 mW to 29 mW with 10.58–24.11 mW output power. Also, the efficiency of HWM circuit changes from 58.81% to 82.49% for the measured output power range. The increase in coupling range and the received power cause the circuit to go into VM. The full wave rectification mode gives the best efficiency values compared to the other two modes. The VM efficiency changes from 82.30% to 89.34%. At the same time output power

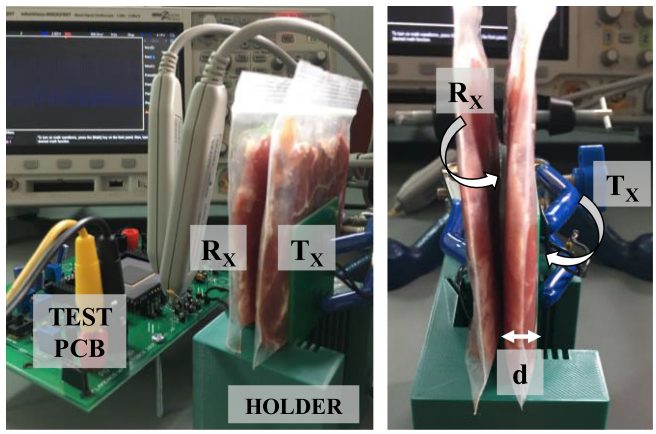

Fig. 19. Experimental setup for inductively coupled coil pair in in vitro tests.

takes values 25.32–51.54 mW for the received signal power of 30.77–57.7 mW. With the proposed triple mode circuit, a wide output power range 233 μW – 51.54 mW is covered. This output power is obtained for the received power range 4 mW – 57.7 mW at the operating frequency of 13.56 MHz.

Analysis of coil pair and the rectifier circuit is performed in air. However, receiver side of the system should be in the human body for medical purposes. Thus, in vitro tests are needed to observe the effects of environment change on the performance of inductive link and the rectifier circuit. The test setup shown in Fig. 19 is used for in vitro experiments. R_X and T_X coils are separated by the coil holder with 6 mm distance (d) . The volume between the coils is filled by air, saline and beef environments

TABLE I
COMPARISON WITH THE STATE OF THE ART

	[9]	[24]	[25]	[16]	[20]	[27]	[28]	**This Work**
Year	2020	2016	2019	2014	2018	2018	2019	**2020**
Technology (µm)	0.18	0.18	0.18	0.35	0.13	0.35	0.18	**0.18**
Active Area (mm^2)	0.853	0.544	0.22	0.0651	0.102	2.4	1.71	**0.9**
Frequency (MHz)	1 - 10	0.05	6.78	13.56	13.56	1	13.56	**13.56**
R_X Architecture	Capacitive Coupling	CM	CM	VM	VM	SVCM[2]	Mixed Mode[3]	**Triple Mode[4]**
R_X Coil Diameter	-	1.17 cm	2 cm	2 cm	2.5 cm	5 cm	2.93 cm	**2.93 cm**
T_X Coil Diameter	-	WE-WPCC	4.8 cm	2 cm	2.5 cm	17 cm	3.45 cm	**3.45 cm**
Coil Distance	-	8.5 cm	-	1.0 cm	1.0 cm	-	5-10 mm	**2-10 mm**
Output Voltage	1.8 – 5 V	1.2 V	1 - 1.2V	1.19 - 3.52 V	2 - 3.46V	3 V	3.3 V	**3.3 V**
P_{OUT} Range	-	-	-	-	-	0.09-18 mW	-	**0.233-51.54 mW**
P_{OUT} (Max.)	231.6 mW	-	15.9 mW	24.8 mW	89 mW	18 mW	112 mW*	**51.54 mW**
PCE (%) @ P_{OUT}	84.4–91.5% (R_L:300Ω) 85.2–91.8% (R_L:100Ω)	67.7 % 2.84 µW[1]	84.7% 15.9 mW	82.2-90.1% (R_L:500Ω) 24.8 mW	88-91.9 % (V_{AC}=3.6 V) RL:100~1kΩ	75 % 18 mW	VM:72.4%* (112 mW)* CM:38.6%* (4.5 mW)*	**CM:51.78 % (8.8 mW) HWM:82.49 % (24.11 mW) VM:89.34 % (51.54 mW)**

[1]Calculated from P_{IN} [3]Mixed Mode: Voltage Mode & Current Mode.
[2]Seamless-voltage-/current-mode [4]Triple Mode: Voltage Mode & Current Mode & Half Wave Mode *Simulation Results.

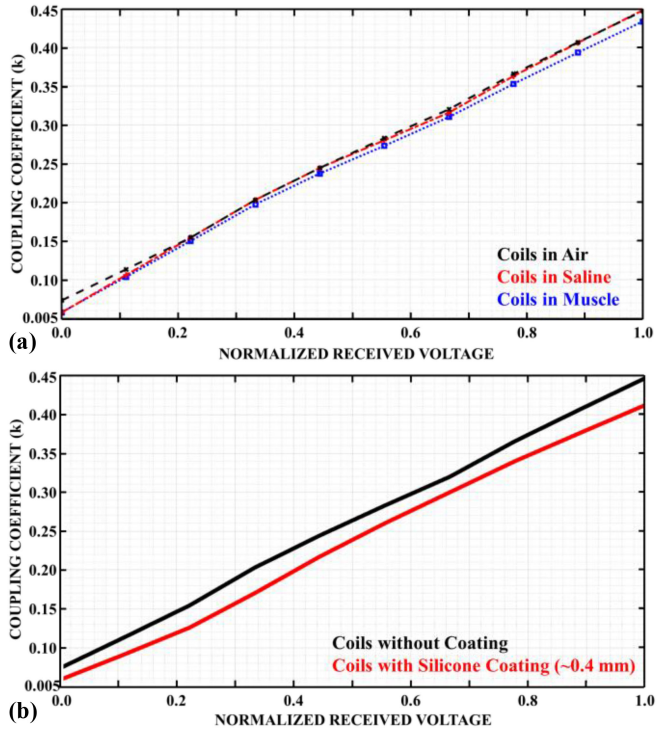

Fig. 20. Coupling coefficient behavior for the normalized receiver voltage (a) in different experiment environments, (b) with and without surface silicone coating on the surface of the coils.

as in [29]. The saline is the solution of distilled water with 9 mg/L NaCl, and the beef is sirloin steak with 6 mm thickness. As Fig. 19 shows the setup for beef, saline solution is also tested with the same way. Another package of saline and beef is also used behind the R_X coil to emulate implant environment. According to experiments, it is observed that coupling coefficient for the normalized received voltage drops slightly when the environment is changed from air to saline and beef (Fig. 20(a)). Triple mode rectifier still can operate in an extended input power range.

Medical devices are coated with biocompatible materials before the end-use. Hence, in addition to environment change, effects of the surface coating of the coils to their performances are analyzed in experiments like [29]. Surface of the PCB coils is coated with ∼0.4 mm silicone. Due to the parasitic effects from the coating material, the value of resonance capacitance of the coils is distorted, and the coupling coefficient decreased compared to uncoated case in air with 6 mm separation distance (Fig. 20(b)). The triple mode rectifier circuit can still operate in each mode with the coated coils. Since the rectifier performance is specified with the receiver side power level, by increasing the voltage level of the transmitter side, this drop can be compensated. As stated in [30], in the RF link performance, surface coating becomes more important than the environment change, and it should be considered to prevent performance drops.

The comparison with the state of the art WPT systems are given in Table I. While all references in the comparison table is about inductive coupling, [9] is based on capacitive coupling WPT method and can be preferred for high power applications. On the contrary, [24] is suitable for very low power applications with 50 kHz frequency in single mode operation. Even if [25] operates at 6.78 MHz frequency, it can charge low voltage batteries. Both [16] and [20] offer rectifier circuits in VM and are limited by high couplings. Although [27] proposes a mixed mode rectifier circuit, coil sizes make the design unsuitable for medical devices. None of these studies combine more than one operation at 13.56 MHz for medical applications. In addition, the performance of most of these studies has been maximized for a single coil distance. However, it cannot be guaranteed to keep the position of the coils fixed during power transmission in the patient body. Therefore, rather than a single point, a distance range should be proposed to compensate possible voltage changes. Operation under different distances corresponds to the extension in the input and output range. For instance, [28] presents a mixed mode rectifier at the operation frequency of 13.56 MHz for medical implants in a distance range. Yet, the efficiency of the circuit is low, and it occupies a larger

area. The proposed work presents a triple mode rectifier circuit which operates with 4 mW – 57.7 mW input range to charge 3.3 V implantable batteries at 13.56 MHz, which is not proposed before. With this novel design, medical implants can be charged without alignment concerns in an extended coupling range.

IV. Conclusion

The implemented triple mode rectifier circuit takes the input through the RF link at the operating frequency 13.56 MHz and converts AC signal to DC voltage in different modes for different coupling levels. For low coupling ratios, caused by misalignment and rotation between the coils, oscillating AC signal is used. In this mode, the charge is accumulated on the receiver coil and transferred to the load in the charging cycle. Full wave rectification is used to perform AC-DC conversion at high couplings. An extended coupling range is covered with the addition of a third mode, called half wave rectifier mode. The symmetry of the design is preserved both in circuit implementation and layout drawings. According to the measurement results of the proposed extended range triple mode rectifier circuit, 0.10–0.42 coupling range is covered for 4 mW – 57.7 mW input power to charge 3.3 V *LOAD* with 0.233–51.54 mW output power range. The maximum efficiency achieved for CM, HWM and VM is 51.78%, 82.49% and 89.34%, respectively. The implemented rectifier circuit can charge the load from 2 mm to 10 mm distance and 0° to 20° angle variations with the maximized efficiency. In vitro experiments show that the RF link and the rectifier circuit can still be utilized for charging the load of the system with the slight drop on the coupling coefficient, which can be compensated by increasing the voltage level of transmitter side within the safe limits. As a future work control block of the system can be supported by another decision unit such as ADC to automize the cycle selection operation in CM. Besides, charge conduction duration of VM and CM can be controlled internally with a feedback circuitry.

Acknowledgment

The authors would like to thank Dr. Hasan Uluşan and Dr. Salar Chamanian for their guidance.

References

[1] F. Zeng, S. Rebscher, W. Harrison, X. Sun, and H. Feng, "Cochlear implants: System design, integration, and evaluation," in *IEEE Rev. Biomed. Eng.*, vol. 1, pp. 115–142, 2008.

[2] B. S. Wilson, "Cochlear implants: Current designs and future possibilities," *J. Rehabil. Res. Dev.*, vol. 45, no. 5, pp. 695–730, 2008.

[3] K. Chen, Y. Lo, Z. Yang, J. D. Weiland, M. S. Humayun, and W. Liu, "A system verification platform for high-density epiretinal prostheses," in *IEEE Trans. Biomed. Circuits Syst.*, vol. 7, no. 3, pp. 326–337, Jun. 2013.

[4] Y.-K. Lo, K. Chen, P. Gad, and W. Liu, "A fully-integrated high-compliance voltage SoC for EPI-retinal and neural prostheses," *IEEE Trans. Biomed. Circuits Syst.*, vol. 7, no. 6, pp. 761–772, Dec. 2013.

[5] S. B. Lee, H.-M. Lee, M. Kiani, U.-M. Jow, and M. Ghovanloo, "An inductively powered scalable 32-channel wireless neural recording system-on-a chip for neuroscience applications," *IEEE Trans. Biomed. Circuits Syst.*, vol. 4, no. 6, pp. 360–371, Dec. 2010.

[6] P. Li and R. Bashirullah, "A wireless power interface for rechargeable battery operated medical implants," *IEEE Trans. Circuits Syst. II Express Briefs*, vol. 54, no. 10, pp. 912–916, Oct. 2007.

[7] R. Erfani, F. Marefat, and P. Mohseni, "Biosafety considerations of a capacitive link for wireless power transfer to biomedical implants," in *Proc. IEEE Biomed. Circuits Syst. Conf.*, 2018, pp. 1–4.

[8] R. Jegadeesan, K. Agarwal, Y.-X. Guo, S.-C. Yen, and N. V. Thakor, "Wireless power delivery to flexible subcutaneous implants using capacitive coupling," *IEEE Trans. Microw. Theory Techn.*, vol. 65, no. 1, pp. 280–292, Jan. 2017.

[9] R. Erfani, F. Marefat, S. Nag, and P. Mohseni, "A 1–10-MHz frequency-aware CMOS active rectifier with dual-loop adaptive delay compensation and >230-mW output power for capacitively powered biomedical implants," *IEEE J. Solid-State Circuits*, vol. 55, no. 3, pp. 756–766, Mar. 2020.

[10] C.-Y. Wu, X.-H. Qian, M.-S. Cheng, Y.-A. Liang, and W.-M. Chen, "A 13.56 MHz 40 mW CMOS high-efficiency inductive link power supply utilizing on-chip delay-compensated voltage doubler rectifier and multiple LDOs for implantable medical devices," *IEEE J. Solid-State Circuits*, vol. 49, no. 11, pp. 2397–2407, Nov. 2014.

[11] A. W. Astrin, H.-B. Li, and R. Kohno, "Standardization for body area networks," *IEICE Trans. Commun.*, vol. E92-B, no. 2, pp. 366–372, 2009.

[12] K. Noh, J. Amanor-Boadu, M. Zhang, and E. Sanchez-Sinencio, "A 13.56-MHz CMOS active rectifier with a voltage mode switched-offset comparator for implantable medical devices," *IEEE Trans. Very Large Scale Integr. Syst.*, vol. 26, no. 10, pp. 2050–2060, Oct. 2018.

[13] H.-M. Lee and M. Ghovanloo, "A high frequency active voltage doubler in standard CMOS using offset-controlled comparators for inductive power transmission," *IEEE Trans. Biomed. Circuits Syst.*, vol. 7, no. 3, pp. 213–224, Jun. 2013.

[14] M. Choi, T. Jang, J. Jeong, S. Jeong, D. Blaauw, and D. Sylvester, "21.5 A current-mode wireless power receiver with optimal resonant cycle tracking for implantable systems," in *Proc. IEEE Int. Solid-State Circuits Conf.*, 2016, vol. 59, pp. 372–373.

[15] Y.-H. Lam, W.-H. Ki, and C.-Y. Tsui, "Integrated low-loss CMOS active rectifier for wirelessly powered devices," *IEEE Trans. Circuits Syst. II Express Briefs*, vol. 53, no. 12, pp. 1378–1382, Dec. 2006.

[16] Y. Lu and W. H. Ki, "A 13.56 MHz CMOS active rectifier with switched-offset and compensated biasing for biomedical wireless power transfer systems," *IEEE Trans. Biomed. Circuits Syst.*, vol. 8, no. 3, pp. 334–344, Jun. 2014.

[17] C. Huang, T. Kawajiri, and H. Ishikuro, "A 13.56-MHz wireless power transfer system with enhanced load-transient response and efficiency by fully integrated wireless constant-idle-time control for biomedical implants," *IEEE J. Solid-State Circuits*, vol. 53, no. 2, pp. 538–551, Feb. 2018.

[18] L. Cheng, W. H. Ki, Y. Lu, and T. S. Yim, "Adaptive on/off delay-compensated active rectifiers for wireless power transfer systems," *IEEE J. Solid-State Circuits*, vol. 51, no. 3, pp. 712–723, Mar. 2016.

[19] C. Huang, T. Kawajiri, and H. Ishikuro, "A near-optimum 13.56 MHz CMOS active rectifier with circuit-delay real-time calibrations for high-current biomedical implants," in *IEEE J. Solid-State Circuits*, vol. 51, no. 8, pp. 1797–1809, Aug. 2016.

[20] H.-C. Cheng, C.-S. A. Gong, and S.-K. Kao, "A 13.56 MHz CMOS high-efficiency active rectifier with dynamically controllable comparator for biomedical wireless power transfer systems," *IEEE Access*, vol. 6, pp. 49979–49989, 2018.

[21] X. Li, C.-Y. Tsui, and W.-H. Ki, "A 13.56 MHz wireless power transfer system with reconfigurable resonant regulating rectifier and wireless power control for implantable medical devices," *IEEE J. Solid-State Circuits*, vol. 50, no. 4, pp. 978–989, Apr. 2015.

[22] L. Cheng, W.-H. Ki, and C.-Y. Tsui, "A 6.78-MHz single-stage wireless power receiver using a 3-mode reconfigurable resonant regulating rectifier," *IEEE J. Solid-State Circuits*, vol. 52, no. 5, pp. 1412–1423, May 2017.

[23] H. S. Gougheri and M. Kiani, "Current-based resonant power delivery with multi-cycle switching for extended-range inductive power transmission," *IEEE Trans. Circuits Syst. I Regular Paper*, vol. 63, no. 9, pp. 1543–1552, Sep. 2016.

[24] M. Choi, T. Jang, J. Jeong, S. Jeong, D. Blaauw, and D. Sylvester, "A resonant current-mode wireless power receiver and battery charger with −32 dBm sensitivity for implantable systems," *IEEE J. Solid-State Circuits*, vol. 51, no. 12, pp. 2880–2892, Dec. 2016.

[25] S.-H. Lee *et al.*, "Voltage-boosted current-mode wireless power receiver for directly charging a low-voltage battery in implantable medical systems," *IEEE Trans. Ind. Electron.*, vol. 66, no. 11, pp. 8860–8865, Nov. 2019.

[26] H. S. Gougheri and M. Kiani, "Self-regulated reconfigurable voltage/current-mode inductive power management," *IEEE J. Solid-State Circuits*, vol. 52, no. 11, pp. 3056–3070, Nov. 2017.

[27] H. Sadeghi Gougheri and M. Kiani, "An inductive voltage-/current-mode integrated power management with seamless mode transition and energy recycling," *IEEE J. Solid-State Circuits*, vol. 54, no. 3, pp. 874–884, Mar. 2019.
[28] Y. Engur, H. Ulusan, H. A. Yigit, S. Chamanian, and H. Kulah, "13.56 MHz mixed mode rectifier circuit for implantable medical devices," in *Proc. 19th Int. Conf. Micro. Nanotechnol. Power Gener. Energy Convers. Appl.*, 2019, pp. 1–4.
[29] U.-M. Jow and M. Ghovanloo, "Modeling and optimization of printed spiral coils in air and muscle tissue environments," in *Proc. IEEE Annu. Int. Conf. Eng. Med. Biol. Soc.*, 2009, pp. 6387–6390.
[30] H. Lee and M. Ghovanloo, "An adaptive reconfigurable active voltage doubler/rectifier for extended-range inductive power transmission," *IEEE Trans. Circuits Syst. II Express Briefs*, vol. 59, no. 8, pp. 481–485, Aug. 2012.

Yasemin Engür (Student Member, IEEE) received the B.Sc. and M.Sc. degrees in electrical and electronics engineering from Middle East Technical University (METU), Ankara, Turkey, in 2018 and 2020, respectively. She is currently a Research Assistant with METU. Her research interests include wireless power transmission, power management circuits, and mixed-signal circuits for wearable and implantable medical applications. During her M.Sc. degree, she was selected as one of the Rising Stars of 2020 by IEEE Solid-State Circuits Society Women in Circuits.

H. Andaç Yiğit received the B.Sc. and M.Sc. degrees in electrical and electronics engineering from Middle East Technical University, Ankara, Turkey, in 2017 and 2020, respectively. His research interests include integrated circuit design, biosensor interfaces, power management circuit, and mixed signal circuits for medical devices.

Haluk Külah (Member, IEEE) received the B.Sc. (Hons.) and M.Sc. (Hons.) degrees from Middle East Technical University (METU), Ankara, Turkey, in 1996 and 1998, respectively, and the Ph.D. degree from the University of Michigan, Ann Arbor, MI, USA, in 2003, all in electrical engineering. During the Ph.D. degree, he worked on micromachined inertial sensors and their interface electronics. From 2003 to 2004, he was a Research Fellow with the Department of Electrical Engineering and Computer Science, University of Michigan. In august 2004, he joined as a Faculty Member with the Electrical and Electronics Engineering Department, METU. He is currently a Board and Executive Committee Member of METU-MEMS Research and Applications Center. His research interests include MEMS, MEMS-based energy scavenging, microsystems for biomedical applications (BioMEMS), and mixed-signal interface electronics design for MEMS sensors. Dr. Külah was the recipient of the 2009 Research Encouragement Award by Prof. Mustafa PARLAR Education and Research Foundation, the 2013 Research Encouragement Award by TÜBİTAK, 2013 IBM Faculty Award, and 2015 Young Scientist Award by Turkish Science Academy. He was the recipient of the EU Horizon 2020 2015 ERC Consolidator Grant by FLAMENCO project and 2020 ERC Proof of Concept Grant by OPERA project, which are on autonomous and fully implantable cochlear implants.